Determination of fluence rate and temperature distributions in the rat brain; implications for photodynamic therapy

Even Angell-Petersen
The Norwegian Radium Hospital
Department of Surgical Oncology
Oslo, Norway N-0310
E-mail: evenag@rr-research.no

Henry Hirschberg
University of California
Beckman Laser Institute
Irvine, California 92617
and
University of Nevada
Department of Health Physics
Las Vegas, Nevada 89154

Steen J. Madsen
University of Nevada
Department of Health Physics and
Cancer Research Center
Las Vegas, Nevada 89154

Abstract. Light and heat distributions are measured in a rat glioma model used in photodynamic therapy. A fiber delivering 632-nm light is fixed in the brain of anesthetized BDIX rats. Fluence rates are measured using calibrated isotropic probes that are positioned stereotactically. Mathematical models are then used to derive tissue optical properties, enabling calculation of fluence rate distributions for general tumor and light application geometries. The fluence rates in tumor-free brains agree well with the models based on diffusion theory and Monte Carlo simulation. In both cases, the best fit is found for absorption and reduced scattering coefficients of 0.57 and 28 cm^{-1}, respectively. In brains with implanted BT_4C tumors, a discrepancy between diffusion and Monte Carlo–derived two-layer models is noted. Both models suggest that tumor tissue has higher absorption and less scattering than normal brain. Temperatures are measured by inserting thermocouples directly into tumor-free brains. A model based on diffusion theory and the bioheat equation is found to be in good agreement with the experimental data and predict a thermal penetration depth of 0.60 cm in normal rat brain. The predicted parameters can be used to estimate the fluences, fluence rates, and temperatures achieved during photodynamic therapy. [DOI: 10.1117/1.2709882]

Keywords: photodynamic therapy; brain tumor; BDIX rat; light dosimetry; tissue optical properties; Monte Carlo simulation.

Paper 06043RR received Mar. 6, 2006; revised manuscript received Sep. 22, 2006; accepted for publication Sep. 22, 2006; published online Feb. 23, 2007. This paper is a revision of a paper presented at the SPIE conference on Lasers in Surgery: Advanced Characterization, Therapeutics, and Systems XIV, Jan. 2004, San Diego, California. The paper presented there appears (unrefereed) in SPIE proceedings Vol. 5316.

1 Introduction

Intracranial light delivery via fiber optics or implanted LED light sources has been used for photodynamic therapy (PDT) in several animal studies.[1–4] PDT is a local treatment involving the administration of a tumor-localizing photosensitizing drug[5] and has several features that make it a potentially attractive adjuvant local therapy for brain tumors. The treatment volume is limited by the attenuation of light in brain tissues, and repeated application is an option due to low long-term morbidity. The probability of achieving local control with PDT therefore depends strongly on the ability to achieve adequate light fluences 1 to 2 cm from the resection margin, where the majority of tumor recurrences occur.[6] PDT has been tested for glioma patients in several clinical trials[7–12] using photosensitizers activated by light with a wavelength around 630 nm. At this wavelength, the light fluence rate decreases[13] exponentially with distance from the resection margin with a light penetration depth of 1 to 3 mm. The penetration depth (distance required to reduce the fluence rate by a factor e^{-1}) of light in brain tissue has been measured *in vivo* for several mammalian species[13–17] and is sensitively dependent on the scattering and absorption properties of the tissue. Accurate knowledge of scattering and absorption coefficients is required to calculate the light distribution for a given geometry in terms of absolute fluence rates. A search of the literature yields large variations in the scattering and absorption coefficients reported for 630-nm light in mammalian brain tissues.[18,19] These discrepancies are likely due to differences in measurement conditions. Furthermore, the accuracy of these values must be questioned since measurements have been performed exclusively on postmortem tissue. Accurate determination of the optical properties of brain tissue requires direct *in situ* measurements.[14]

PDT dosimetry requires knowledge of a number of parameters including light fluence rate. This is particularly important in the brain where damage to eloquent areas can result in severe morbidity. It is possible to measure fluence rates interstitially by inserting isotropic fiber optic probes directly into

Address all correspondence to Even Angell-Petersen, The Norwegian Radium Hospital, Montebello, N-0310 Oslo, Norway; Tel: +47 2293 4000; Fax +47 2293 4270; E-mail: evenag@rr-research.no

1083-3668/2007/12(1)/014003/9/$25.00 © 2007 SPIE

the brain. Studies using either scattering or fluorescent tip probes have been reported in a number of organs,[20–22] but data on absolute fluence rates during interstitial light delivery in mammalian brains are limited. We currently use intracranial light delivery in a rat glioma model to study PDT with the endogenous photosensitizer aminolevulinic acid.[4,23] In this paper, we present *in vivo* measurements of fluence rates around a bare fiber delivering 632-nm light to rat brain and glioma tissue. The measured values in tumor and normal brain were compared to calculated fluence rates obtained from diffusion theory and Monte Carlo simulations, and the comparison yielded estimates of scattering and absorption coefficients. Additionally, temperature profiles were measured by inserting thermocouples directly into the brain, and these measurements were compared to predictions of diffusion theory.

2 Materials and Methods

2.1 *Animal Care*

Animal care and protocol were in accordance with national legislation and institutional guidelines. All animals tested negative for parasitic, bacterial, and viral agents according to Federation of European Laboratory Animal Science Associations (FELASA) recommendations.[24] Inbred BDIX rats (Charles River, Lyon, France) of both sexes weighing 200 to 400 g were caged in pairs or groups of three in Macrolon III cages on a 12-h light and dark schedule. The animal holding rooms and laboratories were maintained at constant temperature and humidity at an air-exchange rate of 18 changes per hour. A total of eight animals were used. Prior to surgery, rats were anesthetized with a standard 1:1 combination of fentanyl/fluanisone (Hypnorm, Janssen, Beerse, Belgium) and midazolam (Dormicum, Roche, Basel, Switzerland). Intracranial tumors were established, as described by Sørensen et al.,[25] by injecting 10,000 BT_4C cells 3 mm into the brain via a burr hole in the skull 3 mm posterior to and 2 mm to the right of the bregma. Tumor-bearing rats were used for experiments 17 days after tumor induction. At that time the tumors had a size of about 4.5 × 6.5 mm centered 3 to 4 mm into the brain, and the animals did not display clinical signs of tumor development. Histopathology of more than 10 rats that were part of other studies[4,23] confirmed that clinical signs occur when the largest tumor diameter is at least 7 mm, and that the tumors at that state are entirely without necrosis. The rats were euthanized immediately after each procedure with a lethal dose of pentobarbitone [100 mg/kg ip (intraperitoneal)].

2.2 *Measurement and Modeling of Light Distributions*

2.2.1 *Isotropic probe for in situ fluence rate measurements*

Small fiber optic isotropic probes, similar to those previously described by Bays et al.,[21] were developed [Fig. 1(a)]. A 250-μm ruby sphere (Sandoz fils SA, Cugy, Switzerland), which is fluorescent under 632-nm light, was glued to a 400 μm/ numerical aperture (NA) 0.37 bare flat-end quartz fiber (Biolitec AG, Jena, Germany) with a UV curable adhesive (Loctite 350, Loctite, Dublin, Ireland). The fiber was covered with thin black polyester tubing (018050 BST, Advanced Polymers Inc., Salem, New Hampshire). Fluorescence from

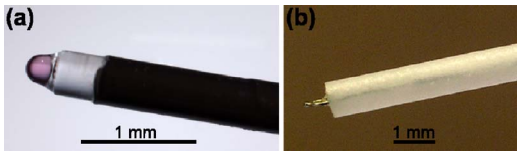

Fig. 1 Image of (a) the fluorescent isotropic probe used for fluence rate measurements and (b) the thermocouple probe used for temperature measurements.

the ruby sphere collected by the fiber was measured with a CCD spectrometer (S2000, OceanOptics Inc., Orlando, Florida) equipped with a 665-nm long-pass filter. A linear combination of the ruby fluorescence spectrum and a third-degree background function, weighted by the spectral response of the system, was fitted to each observed spectrum to quantify the ruby fluorescence and hence the fluence rate. Calibration was done with a setup similar to that described by Marijnissen and Star,[26] with a flat photodiode (S2387-33R, Hamamatsu, Japan) positioned next to the probe in uniform isotropic 632-nm light inside an integrating sphere (Avasphere-50-IRRAD-S, Avantes, Eerbeek, Netherlands) coupled to a diode laser (CeramOptec, Bonn, Germany). The sphere was filled with a 23% sucrose/water solution with a refractive index of 1.37. The spectral response and active area of the photodiode was measured in a National Physical Laboratory (Middlesex, United Kingdom) traceable setup by the Norwegian Metrology Service (Kjeller, Norway), and was corrected for the effects of reflection by the window material (+1.7%) and of measured deviation from the ideal cosine angular response (+1.0%).

2.2.2 *In vivo measurements of intracranial fluence rate distribution*

A plastic template with parallel channels, fitting the light delivery and probe fibers, was used together with a stereotactic frame to control the fiber positions with 0.1-mm precision. The setup is shown in Fig. 2. Anesthetized animals were fixed in the stereotactic frame, the skin was incised, and the frame was used to position the template with the source fiber channel 3 mm posterior to and 2 mm to the right of the bregma.

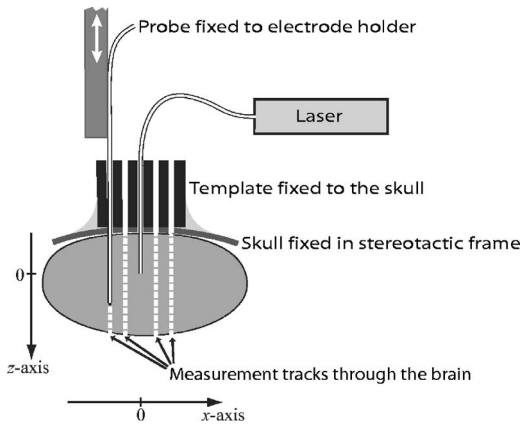

Fig. 2 Setup for the *in vivo* fluence rate measurements. The measurement tracks were positioned within one sagittal plane through the rat brain.

The template was then fixed to the skull using dental cement (Fuji plus, GC, Tokyo, Japan), and the skin closed around the template with sutures to prevent local hypothermia. Holes were drilled through the template channels and into the skull. The light delivery fiber was then inserted into the brain and fixed in the template with histoacryl adhesive (Braun, Melsungen, Germany). The fiber tip delivered 632-nm light from the diode laser at a radiant power of 15 mW. Initial tests of light transmission from the fiber into whole blood and rat brain showed that this radiant power was at least four and seven times, respectively, below the thresholds for heat-induced coagulation. The fluence rate probe was mounted in the stereotactic frame's electrode holder and inserted through the template to record fluence rates along four parallel tracks positioned 2 or 4 mm in front of and behind the light delivery fiber, as shown in Fig. 2. Fluence rates were measured at 0.5-mm increments as the probe was moved into the brain, starting with the tracks 4 mm from the source. The procedure lasted 1 to 2 h, which is comparable to the duration of light exposures in our PDT protocols using BDIX rats.[4]

It was recognized that the probe's black polyester tubing [Fig. 1(a)] could act as a photon sink, resulting in a reduction in the measured signal. To estimate the extent of this perturbation, Monte Carlo simulations were performed for the relevant probe geometry, light penetration depths, and fluence rate gradients. The results show that the black cladding reduces the measured signal by 3 to 25% depending on the fluence rate gradient along the long axis of the probe. These results were used to calculate a general correction factor that was a function of the logarithmic local fluence rate gradient. The maximum correction (corresponding to 25% loss) occurred at the positions where the fluence rate at the cladding was largest compared to the fluence rate at the sphere. For each measurement, the local gradient was estimated using the ratio to the previous measurement in the same measurement series. All measurements were subsequently corrected using their resulting correction factors. The calculation of the corrected fluence rate ϕ can be summarized as

$$\phi(z) = \mathrm{CF}\left[\frac{\tilde{\phi}(z)}{\tilde{\phi}(z - 0.5\ \mathrm{mm})}\right]\tilde{\phi}(z)$$

where $\tilde{\phi}(z)$ is the uncorrected value measured at position z (the geometry is illustrated in Fig. 2), and CF is the correction factor expressed as a function of the ratio.

2.2.3 *Diffusion models of the fluence rate distribution*

According to diffusion theory, the fluence rate ϕ at distance r around an isotropic point source delivering a radiant power P into an infinite turbid medium is approximated by[27]

$$\phi(r) = \frac{P}{4\pi}\frac{3(\mu_s' + \mu_a)\exp(-r/\delta)}{r}, \tag{1}$$

where μ_s' is the reduced scattering coefficient, μ_a is the absorption coefficient, and δ is the light penetration depth:

$$\delta = [3\mu_a(\mu_s' + \mu_a)]^{-1/2}. \tag{2}$$

The presence of a spherical body with differing scattering and absorption coefficients $\mu_{s,\mathrm{tumor}}'$ and $\mu_{a,\mathrm{tumor}}$ and radius R leads to the following solution of the diffusion equation:

$$\phi(r) = \begin{cases} \dfrac{P}{4\pi}\left[C_1\dfrac{\exp(r/\delta_{\mathrm{tumor}})}{r} + C_2\dfrac{\exp(-r/\delta_{\mathrm{tumor}})}{r}\right] & r \le R, \\ \dfrac{P}{4\pi}\left[C_3\dfrac{\exp(-r/\delta)}{r}\right] & r > R, \end{cases} \tag{3}$$

assuming a zero fluence rate at an infinite distance from the source. The constants C_1, C_2, and C_3 follow from conservation of energy, which implies that the output power from the source equals the sum of all optical power absorbed in the medium:

$$P = \int_0^\infty \phi(r)\mu_a 4\pi r^2\,\mathrm{d}r,$$

and from continuity of fluence rate and flux:

$$\phi\big|_{r=R^-} = \phi\big|_{r=R^+},$$

$$\boldsymbol{j}\big|_{r=R^-} = \boldsymbol{j}\big|_{r=R^+},$$

where the flux $\boldsymbol{j}(r)$ is given by the fluence rate[28] as $-[3(\mu_s' + \mu_a)]^{-1}\nabla\phi(r)$. This yields all three constants C_1, C_2, and C_3 as functions of the radius R and the scattering and absorption coefficients of both the spherical body ($\mu_{s,\mathrm{tumor}}'$, $\mu_{a,\mathrm{tumor}}$) and the surrounding medium (μ_s', μ_a).

An anisotropic source can be approximated as an isotropic source displaced a distance $1/(\mu_s' + \mu_a)$ along the direction of the emitted light.[29] In this manner, Eqs. (1) and (3), for tumor-free and tumor-bearing animals, respectively, with r replaced with the distance

$$r = \left[x^2 + \left(z - \frac{1}{\mu_s' + \mu_a}\right)^2\right]^{1/2} \tag{4}$$

were used to model the fluence rate at horizontal distance x and vertical distance z from the fiber tip. These models for the fluence rate $\phi(z,x)$ were fitted to the *in vivo* fluence rate measurements by log-weighted least-squares estimation (Marquardt-Levenberg algorithm), to estimate the tissue optical properties μ_s', μ_a, $\mu_{s,\mathrm{tumor}}'$, and $\mu_{a,\mathrm{tumor}}$.

2.2.4 *Monte Carlo model of the fluence rate distribution*

A commonly used Monte Carlo code[†30] was modified for the light delivery geometry in the animals. The fiber tip was modeled as a 400-μm disk emitting a conical photon beam of ±9 deg, and the brain was considered to be an infinite medium with uniform scattering and absorption properties. Anisotropic scattering was modeled using a Henyey-Greenstein phase function with scattering anisotropy (g) values of be-

[†]Available online at http://omlc.ogi.edu/software/mc/small_mc.c.

tween 0.8 and 0.98, which is the range of values reported for tissues.[18,19,31,32] Tumors were modeled as ellipsoids with varying scattering and absorption coefficients, and with their size and position determined from histological sections of brains from tumor-bearing animals. The Monte Carlo simulations were fit to measured fluence rates using an optimization algorithm that systematically varied the absorption and scattering coefficients to find the best least-squares estimate. About 500,000 runs, requiring 30 min on a 3.6-GHz Pentium 4 processor, were necessary for each set of coefficients to achieve an accuracy of 2%.

2.3 *Measurement and Modeling of Temperature Distributions*

2.3.1 *In vivo measurements of intracranial temperature distributions*

Temperature measurements in tumor-free animals were accomplished by inserting thermocouples into the rat brain. The thermocouple probes are shown in Fig. 1(b), and were assembled from K-type 75-μm wire thermocouples (CHAL-003, Omega Engineering, Stamford, Connecticut) mounted in 800-μm ceramic tubing (TRA-005132, Omega Engineering, Stamford, Connecticut). The probes were tested immersed in water under a laser beam to verify that direct light absorption in the thermocouple did not affect the readings. No noticeable increase related to direct absorption was observed for fluence rates below 0.25 W cm^{-2}, and at 1.2 W cm^{-2}, the increase was only 0.2 K. To account for subtle changes in body temperature, all measurements were normalized to rectal body temperature monitored with a 0.5-mm insulated thermocouple. In the rat brain, positioning of the thermocouples with respect to the source fiber was accomplished in a similar manner as that described for the fluence rate measurements in Sec. 2.2.2. Two distinct data sets were collected from each animal: First, steady state temperatures elevated by the light delivery were measured at 0.5-mm increments as the probe was moved into the brain. The temperature increase caused by light absorption was then estimated by subtracting steady state temperatures measured while no light was delivered from the fiber tip during the withdrawal of the temperature probe. Second, temporal measurements of temperature increase and decrease (as the laser light was switched on and off, respectively) were made during the withdrawal of the probe, with the probe fixed 2 mm lateral to the source fiber tip.

2.3.2 *Bioheat model of the temperature distribution*

From the bioheat equation[33] and Eq. (1), the temperature increase T in tissue around a point source is described by

$$\frac{\partial T}{\partial t} = \frac{\kappa}{\rho c}\nabla^2 T - QT + \frac{P}{4\pi}\frac{\exp(-r/\delta)}{\kappa\delta^2 r}, \tag{5}$$

where κ is the heat conductivity, ρ is the density, c is the specific heat capacity, and Q is the blood perfusion rate. To model the spatial temperature distribution, the steady state solution to Eq. (5),

$$T(r) = \frac{P}{4\pi}\frac{\exp(-r/\delta_v) - \exp(-r/\delta)}{\kappa\left(1 - \frac{\delta^2}{\delta_v^2}\right)r}, \tag{6}$$

was fitted to the spatial measurement series. The thermal penetration depth $\delta_v = [\kappa/(Q\rho c)]^{1/2}$ was used as a free parameter, while a heat conductivity of 0.53 W m^{-1} K^{-1} (Ref. 34) was assumed. Equation (4) was substituted into Eq. (6) to correct for the distance to the anisotropic source. The temporal temperature variation was modeled using the time-dependent Eq. (5). For this purpose, Eq. (5) was solved numerically for different δ_v values, using a finite difference method with explicit time stepping,[35] to find the best least-squares fit to the temporal measurements.

3 Results

3.1 *Light Distribution*

3.1.1 *Measured fluence rates in the rat brain*

Fluence rate measurements from four tumor-free rats are shown in Fig. 3(a). (A preliminary analysis of the results from two of the rats was published in a previous report.[36]) Inter- and intraanimal variation was of similar magnitude. As seen from the data series in the diagrams in Fig. 3, the measured fluence rates throughout the brains were consistent within a total variability of a factor of 2. There was relatively good agreement between diffusion theory [Eqs. (1), (2), and (4)] and the measured data. The best fit was found for $\mu_a = 0.570$ cm^{-1} (standard error 0.021 cm^{-1}) and $\mu_s' = 27.9$ cm^{-1} (standard error 2.4 cm^{-1}), and is shown as solid lines in Fig. 3(a). These values correspond to a light penetration depth of 0.143 cm [Eq. (2)]. Measurements made closer than 2 mm from the skull were excluded from the analysis.

Results of measurements from two tumor-bearing rats with fibers positioned 1 to 2 mm above the tumor centers are shown in Fig. 3(b). The recorded fluence rates were significantly lower than in the tumor-free brains, particularly in the area closest to the fiber tip where the values were reduced by a factor of 2. Furthermore, the light distribution was shifted about one millimeter away from the fiber tip (i.e., z direction in Fig. 3), suggesting that the tumor tissue in front of the fiber tip had a lower scattering coefficient than normal brain. The diffusion theory model [Eq. (3)], with tumor radius $R = 2.5$ mm and the already mentioned scattering and absorption coefficients from tumor-free animals, was fitted to the measured fluence rates. As we see in Fig. 3(b) there is good agreement between the model and the experimental data. The best fit was found for $\mu_{a,\text{tumor}} = 1.46$ cm^{-1} (standard error 0.094 cm^{-1}) and $\mu_{s,\text{tumor}}' = 5.45$ cm^{-1} (standard error 0.44 cm^{-1}). This corresponds to a light penetration depth of 0.181 cm [Eq. (2)].

3.1.2 *Fluence rates estimated by Monte Carlo simulation*

As expected, in media where scattering dominates absorption, the distributions calculated by Monte Carlo simulation were closely related to the diffusion theory model. For tumor-free rat brain, the absorption and scattering coefficients yielding the best least-squares fit to the measured fluence rates did not deviate from the diffusion model estimates (i.e., the deviation

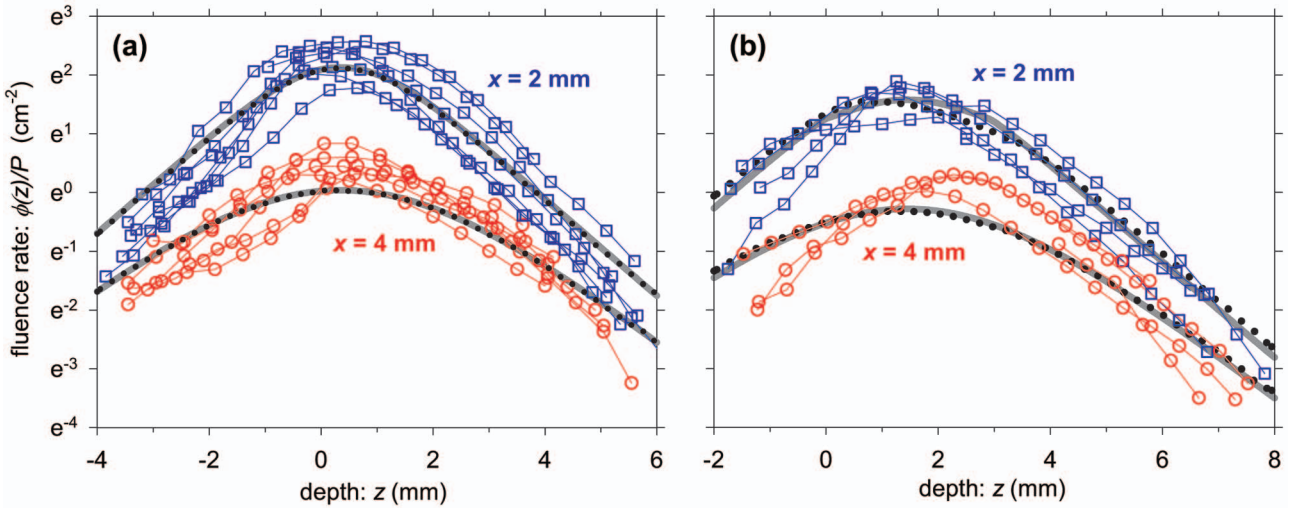

Fig. 3 Interstitial fluence rate ϕ relative to radiant power P plotted as a function of vertical distance z and lateral distance x from the source fiber tip. The geometry and coordinates are illustrated in Fig. 2. (a) Data from four tumor-free rats with the source fiber fixed 4 to 4.5 mm into the brain and (b) data from two tumor-bearing rats with the source fiber fixed 2 mm into the brain. Measurement series were recorded along tracks positioned parallel to the source fiber at $x=\pm 2$ mm (□) and $x=\pm 4$ mm (○). The thick solid lines represent diffusion theory predictions [Eqs. (1) to (4)] fitted to the measured fluence rates, omitting measurements made less than 2 mm from the skull. Correspondingly, the dotted lines are the best fit of the Monte Carlo model. The fluorescent probes were somewhat fragile, and therefore three measurement series in (a) and one (in part) in (b) are absent. The data in the diagrams are corrected using the method described in Sec. 2.2.2.

was less than the 2% optimization accuracy described in Sec. 2.2.4). At positions along the measurement tracks (Fig. 2), the Monte Carlo model predicted fluence rates almost identical to diffusion theory. Likewise, as expected when diffusion theory is valid, variation of the scattering anisotropy had no significant effect. In general, major fluence rate discrepancies between Monte Carlo simulations and diffusion theory were seen exclusively at positions within 0.5 mm from the source fiber tip, where no experimental data were recorded.

More pronounced differences between the diffusion model and Monte Carlo simulations were observed in tumor-bearing animals. The tumor was modeled as a 6.5 × 4.5-mm ellipsoid centered 1.5 mm below the fiber tip, embedded in normal brain with the scattering and absorption coefficients estimated from measurements in tumor-free animals. The best least-squares fit to the measured fluence rates was found for $\mu_{a,\text{tumor}}=1.39\ \text{cm}^{-1}$ and $\mu'_{s,\text{tumor}}=7.3\ \text{cm}^{-1}$, and is shown in Fig. 3(b). These values deviate from the diffusion theory results already determined and correspond to a shorter light penetration depth of 0.166 cm. A map of the light distributions predicted by Monte Carlo simulation and diffusion theory for a given tumor shape and set of optical properties is shown in Fig. 4. Such comparisons showed that, although the models yielded similar results in the normal brain at distances in excess of 3 to 4 mm from the fiber tip, the diffusion model overestimated the fluence rate in large parts of the tumor by 30 to 50% compared to the Monte Carlo model. The scattering anisotropy did not have much effect on the Monte Carlo model. Variation of the anisotropy value g within the range 0.8 and 0.99 shifted the isodose contours shown in Fig. 4 by less than 0.1 mm.

Monte Carlo simulations featuring 100% reflecting or absorbing surfaces at the positions of the skull were performed to investigate finite volume effects. As shown in Fig. 5, the fluence rate at the measured positions was altered by less than 5% as long as sites closer than 2 mm to the surface were omitted. The skull and its surrounding soft tissues have optical properties of similar order of magnitude as the brain,[18] and should represent far lower perturbations than the 100% reflecting or absorbing surfaces.

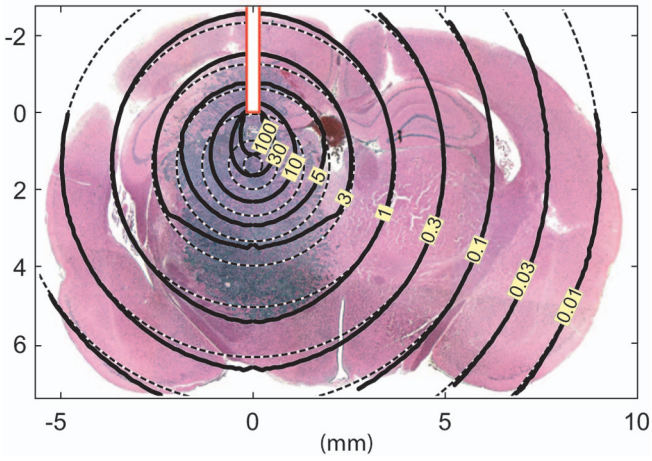

Fig. 4 Distribution of light in tumor-bearing rat brain. The contours show fluence rate ϕ relative to the radiant power P emitted from a bare fiber tip (unit: inverse centimeters squared). The solid lines are calculated by Monte Carlo simulations for an ellipsoid 4.5 × 6.5-mm tumor geometry and optical properties $\mu_a=0.62\ \text{cm}^{-1}$, $\mu'_s=31\ \text{cm}^{-1}$, $\mu_{a,\text{tumor}}=1.6\ \text{cm}^{-1}$, $\mu'_{s,\text{tumor}}=7.7\ \text{cm}^{-1}$, and $g=0.90$. The dotted lines are the corresponding contours according to the diffusion theory model [Eqs. (3) and (4)] with the same optical properties and the tumor approximated as a 2.5-mm-radius sphere.

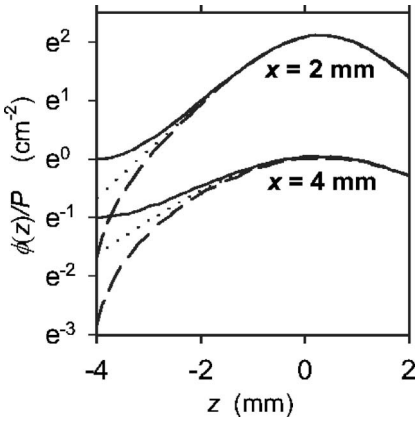

Fig. 5 Fluence rates calculated by the Monte Carlo model featuring worst-case finite volume effects. The lines represent 100% reflecting (—) and absorbing (- - -) surfaces added at $z=-4$ mm to the geometry presented in Fig. 3. The dotted lines represent the ideal infinite geometry.

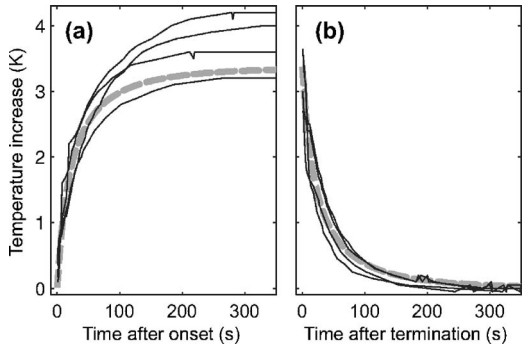

Fig. 7 Temperature change after (a) onset and (b) termination of 100 mW of light input. The diagrams show the increase above steady state temperature with no light input. The temperature was recorded at perpendicular positions 2 mm lateral to the fiber tip ($x=\pm 2$ mm and $z=0$ in Fig. 2) in two rats. Each solid line shows data from one measurement series. The thick dashed lines are the bioheat model [Eq. (5)] fitted to all measurements.

3.2 *Measured Temperatures in the Rat Brain*

Temperatures around the source fiber were measured in two tumor-free rats. Background measurements made in the absence of laser light showed a significant gradient, with temperatures starting at 2.1 to 3.5 K below rectal body temperature (33.1 to 35.1°C) in the most superficial layers of the brain, and reaching rectal body temperature 7 to 9 mm into the brain. Interstitial delivery of 100 mW of light caused elevated temperatures detectable more than 6 mm from the source fiber tip. At positions 2 mm lateral to the fiber tip the increase was 3.5 to 4.0 K at steady state. The variation within measurements made at equivalent positions was mostly less than 0.5 K. As we see in Fig. 6, the steady state model described by Eq. (6) was in good agreement with measured temperature increases. The best fit was found for a thermal penetration depth of $\delta_v=0.60$ cm (standard error 0.02 cm) if δ was fixed at 0.143 cm as estimated from the fluence rate measurements (see Sec. 3.1.1). Similar values of $\delta_v=0.58$ cm and $\delta=0.137$ cm were found if both variables were used as free parameters. Extrapolation of Eq. (6) using these parameters yields a temperature increase of 8.5 K at the fiber tip.

An alternative estimate of the thermal penetration depth was found by fitting the time dependent bioheat Eq. (5) to the temporal temperature measurements recorded at fixed positions 2 mm lateral to the fiber tip. These temporal temperature changes following onset and termination of light input are shown in Fig. 7. Numerical solutions of the bioheat equation [Eq. (5)] were in good agreement with the data, particularly for the temperature decrease following light termination [Fig. 7(b)], and the best fit was found for a thermal penetration depth $\delta_v=0.51$ cm.

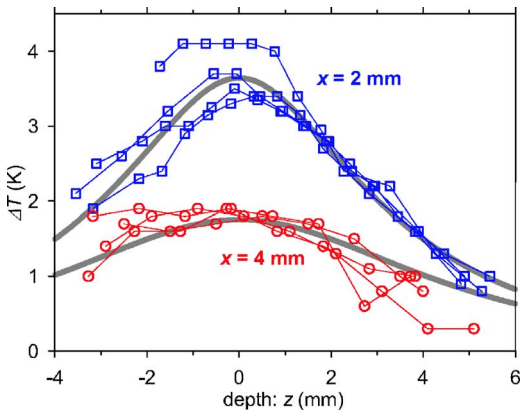

Fig. 6 Spatial distribution of steady state temperature increase during light exposure. The geometry and coordinates are illustrated in Fig. 2. The symbols show the difference between the temperature measured with 100 mW of input power and the local temperature measured with no light input. Measurement series were recorded in two rats along tracks positioned parallel to the source fiber at $x=\pm 2$ mm (□) and $x=\pm 4$ mm (○). The source fibers were fixed 4 mm into the brain. The thick solid lines are the steady state bioheat model [Eq. (6)] fitted to the measured temperature.

4 Discussion

The *in vivo* measurements yielded the tissue optical parameters: $\mu_a=0.57$ cm^{-1}, $\mu_s'=28$ cm^{-1}, and $\delta=0.14$ cm for 632-nm light in rat brain tissue. This is in good agreement with other *in vivo* measurements of δ in mammalian brains, which have been found[13–17] to be within the range 0.10 to 0.27 cm. To our knowledge, *in vivo* measurements of the absorption and scattering coefficients at this wavelength have not been reported, but values determined from extracted tissues have been[18,19,32,37–40] within the ranges $\mu_a=0.20$ to 2.7 cm^{-1} and $\mu_s'=6.4$ to 100 cm^{-1}. Unlike absorption, scattering does not depend strongly on wavelength: μ_s' has been reported[19,38–40] to decrease by less than 20% as the wavelength increases from 632 nm and into the near-IR, where *in vivo* measurements have been performed with diffuse reflectance probes. In the human brain Bevilacqua et al. have found[41] $\mu_s'=10$ cm^{-1} for gray matter and $\mu_s'=14$ cm^{-1} for white matter at 674 nm. In better agreement with this study, higher values were reported for rat brain by Johns et al.,[42] who found $\mu_s'=12$ to 25 cm^{-1} in gray matter and $\mu_s'=35$ to 60 cm^{-1} in white matter at 750 nm. The white matter struc-

tures in the rat brain are typically less than 1 mm thick and therefore constitute just 7 to 10% of the volume interrogated by the light fields in this study.[43] Hence, the presented estimates are best interpreted as optical properties of gray matter. The estimated δ correspond to a 1000-fold decrease in fluence rate over a 1-cm distance through rat gray matter. However, since most tumors in patients arise and infiltrate in white matter the high attenuation of light at 632 nm in gray matter does not necessarily represent a clinically imposing problem. The measurements by Muller and Wilson[13] indicate a more favorable penetration in actual resection margins where the tissue is a mixture of brain and tumor tissue.

For tumor tissue, there was some discrepancy between the diffusion and Monte Carlo models. The Monte Carlo estimates are considered to be more accurate, since the exact geometry (tumor shape, fiber position, and the nonisotropic source) can easily be represented, and since discrepancies due to limitations of the diffusion approximation are expected for the relatively small difference between $\mu_{a,\mathrm{tumor}}$ and $\mu'_{s,\mathrm{tumor}}$. The optical properties were estimated from only two animals, and this makes the values less reliable than those measured in tumor-free brain. Still, both the observed displacement along the z axis and the average reduction in fluence rate (as seen in Fig. 3) were distinct compared to the interanimal variability. This suggests that there are differences in the optical properties of tumor tissue and normal brain. As illustrated in Fig. 4, the estimates can be useful when evaluating light dosimetry for the BT_4C tumor model. However, measurements in additional animals will be required for a more accurate determination of the optical properties of glioma tissue.

The large number of measurements should rule out the possibility that small structures, like blood vessels or ventricles, affected the predicted light distributions. Still, inhomogeneities may have been the major cause of the twofold variability seen in Fig. 3. The most noteworthy deviation between the measured and the modeled fluence rate is seen in Fig. 3 for the region 4 mm lateral to the source fiber tip in both tumor-free [Fig. 3(a)] and tumor-bearing [Fig. 3(b)] brains. The predicted fluence rates (the lower solid lines in the diagrams) around the peak positions seem low compared to the measurements, implying an overestimation of light attenuation. There is no obvious explanation for this discrepancy, but it could be related to local variations in optical properties.

The sources of error are complex and therefore it is difficult to evaluate the uncertainty in the estimates of μ_a, μ'_s, and δ. Calibration of the fluence rate probes can be a major source of error. Ideally, the probes should be calibrated in a medium similar to rat brain, rather than in a clear solution, because the probe may perturb the fluence rate of its surroundings in a scattering- and absorption-dependent manner.[44] In the presented case, such perturbation was probably minor due to the small probe dimensions. Furthermore, calculations using the multilayer Monte Carlo software[45] MCML indicated that infinite layers of ruby or silica, with thicknesses comparable to the respective dimensions in the probes, would alter the fluence rate in adjacent brain tissue by less than 5%. The small ruby and silica structures in the probes would without doubt perturb far less than infinite layers. As described in Sec. 2.2.2, the black fiber tubing close to the fluorescent sphere affected the measurements, but the applied correction factor based on Monte Carlo simulations essentially eliminated this artifact. Additional simulations featuring relevant variations in the absorption of the tubing and the light penetration depth in rat brain suggested that those factors do not alter the correction factor significantly. It is clear from Eq. (1) that both μ'_s and μ_a are sensitive to probe calibration errors, but fortunately they are estimated by utilizing both the absolute magnitude of the fluence rate [Eq. (1)] and the displacement of the light distribution along the z axis [Eq. (4)]. The fact that the model fits the data in terms of both absolute fluence rate and z offset simultaneously [Fig. 3(a)] strengthens the reliability of the estimated μ'_s and μ_a.

The measured temperature distribution shown in Fig. 6 is in good agreement with the predictions of the steady state bioheat model [Eq. (6)]. The model yielded similar thermal penetration depths (δ_v) when fitted to the experimental data in both spatial (Fig. 6) and time domains (Fig. 7). This implies that this simple model is adequate for describing the temperature increase during interstitial light delivery with a bare fiber tip. Furthermore, sound estimates of both δ and δ_v were found when δ as used as a free parameter instead of being fixed at the value found from the fluence rate measurements. The thermal penetration depth is directly related to blood flow (as defined in Sec. 2.3.2). The measured thermal penetration depth of 0.51 to 0.60 cm corresponds to a blood flow of 0.23 to 0.32 mL min^{-1} g^{-1}, if a heat capacity of 3.7 kJ kg^{-1} K^{-1} and a density of 1.03 g mL^{-1} are assumed.[46] This flow rate is 2 to 4 times less than that reported elsewhere for rat gray matter,[47] which means that both the gradient in the spatial measurements and the rate of change in the temporal measurements were lower than one would expect from the literature. The reduction can, at least in part, be explained by well-known effects of the applied anesthesia on cerebral perfusion.[48] In addition, finite volume effects from ambient air, bone, muscle, and skin, which is less perfused,[49,50] may have elevated the temperature in the brain, resulting in an overestimation of the thermal penetration depth and hence, underestimation of perfusion. The finite volume effect of the top tissue-to-air surface is also a plausible cause for the distinct asymmetry seen in Fig. 6, where the temperature is elevated closest to the top surface (i.e., for $z<0$). The initial tests of direct light absorption in the thermocouple (Sec. 2.3.1) suggests that this artifact increased the temperature readings closest to the source by 0.2 K, which is a minor aberration compared to the observed spatial and temporal temperature spans.

In conclusion, the distributions of light and heat during interstitial light delivery were successfully mapped using *in situ* measurements and mathematical modeling. Optical properties were derived, and can be used to predict fluence rate distributions during PDT in rat brain. The fluence rate distribution was found to be predictable, and could be estimated by diffusion theory in tumor-free brains and by Monte Carlo simulations in tumor-bearing brains. The presence of a tumor altered the light distribution significantly, and the models suggested that the tumor had higher absorption and lower scattering than normal brain. Rat brain was found to have absorption and reduced scattering coefficients of 0.57 and 28 cm^{-1}, respectively. These coefficients have, to our knowledge, not been reported for comparable wavelengths *in vivo*, but the

resulting penetration depth of 0.14 cm is in agreement with numerous *in vivo* studies in the literature. The temperature measurements showed that the extent of heating during interstitial light delivery could be modeled with a regular point source diffusion model. The findings of the study make it feasible to predict the fluences, fluence rates, and temperatures achieved during intracranial photodynamic therapy.

Acknowledgments

We would like to thank Jørn Iversen for his work at the instrument workshop; Roland Bays and Lise Lyngsnes Randeberg for useful tips regarding the fluence rate probes and the temperature measurements, respectively; and Dag Sørensen at the Centre for Comparative Medicine at Rikshospitalet for help with the animal work. The BT_4C cell line was provided by Rolf Bjerkvig at the University of Bergen.

References

1. L. Lilge, M. C. Olivo, S. W. Schatz, J. A. MaGuire, M. S. Patterson, and B. C. Wilson, "The sensitivity of normal brain and intracranially implanted VX2 tumour to interstitial photodynamic therapy," *Br. J. Cancer* **73**, 332–343 (1996).
2. J. Lobel, I. J. MacDonald, M. J. Ciesielski, T. Barone, W. R. Potter, J. Pollina, R. J. Plunkett, R. A. Fenstermaker, and T. J. Dougherty, "2-[1-hexyloxyethyl]-2-devinyl pyropheophorbide-a (HPPH) in a nude rat glioma model: implications for photodynamic therapy," *Lasers Surg. Med.* **29**, 397–405 (2001).
3. S. K. Bisland, L. Lilge, A. Lin, R. Rusnov, and B. C. Wilson, "Metronomic photodynamic therapy as a new paradigm for photodynamic therapy: rationale and preclinical evaluation of technical feasibility for treating malignant brain tumors," *Photochem. Photobiol.* **80**, 22–30 (2004).
4. E. Angell-Petersen, S. Spetalen, S. J. Madsen, C.-H. Sun, Q. Peng, S. W. Carper, M. Sioud, and H. Hirschberg, "Influence of light fluence rate on the effects of photodynamic therapy in an orthotopic rat glioma model," *J. Neurosurg.* **104**, 109–117 (2006).
5. T. J. Dougherty, C. J. Gomer, B. W. Henderson, G. Jori, D. Kessel, M. Korbelik, J. Moan, and Q. Peng, "Photodynamic therapy," *J. Natl. Cancer Inst.* **90**, 889–905 (1998).
6. K. E. Wallner, J. H. Galicich, G. Krol, E. Arbit, and M. G. Malkin, "Patterns of failure following treatment for glioblastoma multiforme and anaplastic astrocytoma," *Int. J. Radiat. Oncol., Biol., Phys.* **16**, 1405–1409 (1989).
7. E. A. Popovic, A. H. Kaye, and J. S. Hill, "Photodynamic therapy of brain tumors," *Semin Surg. Oncol.* **11**, 335–345 (1995).
8. P. J. Muller and B. C. Wilson, "Photodynamic therapy for recurrent supratentorial gliomas," *Semin Surg. Oncol.* **11**, 346–354 (1995).
9. P. J. Muller and B. C. Wilson, "Photodynamic therapy for malignant newly diagnosed supratentorial gliomas," *J. Clin. Laser Med. Surg.* **14**, 263–270 (1996).
10. S. Krishnamurthy, S. K. Powers, P. Witmer, and T. Brown, "Optimal light dose for interstitial photodynamic therapy in treatment for malignant brain tumors," *Lasers Surg. Med.* **27**, 224–234 (2000).
11. M. A. Rosenthal, B. Kavar, S. Uren, and A. H. Kaye, "Promising survival in patients with high-grade gliomas following therapy with a novel boronated porphyrin," *Clin. Neurosci.* **10**, 425–427 (2003).
12. S. S. Stylli, M. Howes, L. MacGregor, P. Rajendra, and A. H. Kaye, "Photodynamic therapy of brain tumours: evaluation of porphyrin uptake versus clinical outcome," *Clin. Neurosci.* **11**, 584–596 (2004).
13. P. J. Muller and B. C. Wilson, "An update on the penetration depth of 630 nm light in normal and malignant human brain tissue in vivo," *Phys. Med. Biol.* **31**, 1295–1297 (1986).
14. B. C. Wilson, W. P. Jeeves, and D. M. Lowe, "In vivo and post mortem measurements of the attenuation spectra of light in mammalian tissues," *Photochem. Photobiol.* **42**, 153–162 (1985).
15. D. R. Doiron, L. O. Svaasand, and A. E. Profio, "Light dosimetry in tissue applications to photoradiation therapy," in *Porphyrin Photosensitization*, D. Kessel and T. J. Dougherty, Eds., pp. 63–75, Plenum Press, New York (1983).
16. S. K. Powers and J. T. Brown, "Light dosimetry in brain tissue: an in vivo model applicable to photodynamic therapy," *Lasers Surg. Med.* **6**, 318–322 (1986).
17. Q. Chen, M. Chopp, L. Madigan, M. O. Dereski, and F. W. Hetzel, "Damage threshold of normal rat brain in photodynamic therapy," *Photochem. Photobiol.* **64**, 163–167 (1996).
18. W. F. Cheong, "Summary of optical properties," in *Optical-Thermal Response of Laser-Irradiated Tissue*, A. J. Welch and M. J. van Gemert, Eds., pp. 275–303, Plenum Press, New York (1995).
19. A. N. Yaroslavsky, P. C. Schulze, I. V. Yaroslavsky, R. Schober, F. Ulrich, and H. J. Schwarzmaier, "Optical properties of selected native and coagulated human brain tissues in vitro in the visible and near infrared spectral range," *Phys. Med. Biol.* **47**, 2059–2073 (2002).
20. L. Lilge, T. Haw, and B. C. Wilson, "Miniature isotropic optical fibre probes for quantitative light dosimetry in tissue," *Phys. Med. Biol.* **38**, 215–230 (1993).
21. R. Bays, G. Wagnieres, D. Robert, J. F. Theumann, A. Vitkin, J. F. Savary, P. Monnier, and H. van den Bergh, "Three-dimensional optical phantom and its application in photodynamic therapy," *Lasers Surg. Med.* **21**, 227–234 (1997).
22. T. C. Zhu, A. Dimofte, J. C. Finlay, D. Stripp, T. Busch, J. Miles, R. Whittington, S. B. Malkowicz, Z. Tochner, E. Glatstein, and S. M. Hahn, "Optical properties of human prostate at 732 nm measured in mediated photodynamic therapy," *Photochem. Photobiol.* **81**, 96–105 (2005).
23. S. J. Madsen, E. Angell-Petersen, S. Spetalen, S. W. Carper, S. A. Ziegler, and H. Hirschberg, "Photodynamic therapy of newly implanted glioma cells in the rat brain," *Lasers Surg. Med.* **38**, 540–548 (2006).
24. C. Rehbinder, P. Baneux, D. Forbes, H. van Herck, W. Nicklas, Z. Rugaya, and G. Winkler, "FELASA recommendations for the health monitoring of mouse, rat, hamster, gerbil, guinea pig and rabbit experimental units. Report of the Federation of European Laboratory Animal Science Associations (FELASA) Working Group on Animal Health accepted by the FELASA Board of Management, November 1995," *Lab Anim.* **30**, 193–208 (1996).
25. D. R. Sørensen, T. A. Read, T. Porwol, B. R. Olsen, R. Timpl, T. Sasaki, P. O. Iversen, H. B. Benestad, B. K. Sim, and R. Bjerkvig, "Endostatin reduces vascularization, blood flow, and growth in a rat gliosarcoma," *Neuro.-Oncol.* **4**, 1–8 (2002).
26. J. P. Marijnissen and W. M. Star, "Calibration of isotropic light dosimetry probes based on scattering bulbs in clear media," *Phys. Med. Biol.* **41**, 1191–1208 (1996).
27. I. Driver, C. P. Lowdell, and D. V. Ash, "In vivo measurement of the optical interaction coefficients of human tumours at 630 nm," *Phys. Med. Biol.* **36**, 805–813 (1991).
28. R. C. Haskell, L. O. Svaasand, T. T. Tsay, T. C. Feng, M. S. McAdams, and B. J. Tromberg, "Boundary conditions for the diffusion equation in radiative transfer," *J. Opt. Soc. Am. A* **11**, 2727–2741 (1994).
29. S. L. Jacques, "Light distributions from point, line and plane sources for photochemical reactions and fluorescence in turbid biological tissues," *Photochem. Photobiol.* **67**, 23–32 (1998).
30. S. A. Prahl, M. Keijzer, S. L. Jacques, and A. J. Welch, "A Monte Carlo model of light propagation in tissue," in *Dosimetry of Laser Radiation in Medicine and Biology*, G. J. Mueller and D. H. Sliney, Eds., *Proc. SPIE*, **IS 5**, 102–111 (1989).
31. R. Splinter, W. F. Cheong, M. J. van Gemert, and A. J. Welch, "In vitro optical properties of human and canine brain and urinary bladder tissues at 633 nm," *Lasers Surg. Med.* **9**, 37–41 (1989).
32. B. C. Wilson, M. S. Patterson, and D. M. Burns, "Effect of photosensitizer concentration in tissue on the penetration depth of photoactivating light," *Lasers Med. Sci.* **1**, 235–244 (1986).
33. H. H. Pennes, "Analysis of tissue and arterial blood temperature in the resting human forearm," *J. Appl. Physiol.* **1**, 93–122 (1948).
34. T. E. Cooper and G. J. Trezek, "Correlation of thermal properties of some human tissue with water content," *Aerosp. Med.* **42**, 24–27 (1971).
35. W. J. Minkowycz, E. M. Sparrow, G. E. Schneider, and R. H. Pletcher, *Handbook of Numerical Heat Transfer*, Wiley, New York (1988).
36. E. Angell-Petersen, D. R. Sørensen, S. J. Madsen, and H. Hirschberg, "Interstitial light application for photodynamic therapy in a rat brain tumor model," *Proc. SPIE* **5312**, 415–423 (2004).
37. S. T. Flock, B. C. Wilson, and M. S. Patterson, "Total attenuation coefficients and scattering phase functions of tissues and phantom

materials at 633 nm," *Med. Phys.* **14**, 835–841 (1987).
38. J. L. Karagiannes, Z. Zhang, and L. I. Grossweiner, "Applications of the 1D diffusion approximation to the optics of tissues and tissue phantoms," *Appl. Opt.* **28**, 2311–2317 (1989).
39. H. J. C. M. Sterenborg, M. J. van Gemert, W. Kamphorst, J. G. Wolbers, and W. Hogervorst, "The spectral dependence of the optical properties of human brain," *Lasers Med. Sci.* **4**, 221–227 (1989).
40. P. van der Zee, M. Essenpreis, and D. T. Delpy, "Optical properties of brain tissue," *Proc. SPIE* **1888**, 454–465 (1993).
41. F. Bevilacqua, D. Piguet, P. Marquet, J. D. Gross, B. J. Tromberg, and C. Depeursinge, "In vivo local determination of tissue optical properties: applications to human brain," *Appl. Opt.* **38**, 4939–4950 (1999).
42. M. Johns, C. A. Giller, D. C. German, and H. L. Liu, "Determination of reduced scattering coefficient of biological tissue from a needle-like probe," *Opt. Express* **13**, 4828–4842 (2005).
43. G. Paxinos and C. Watson, *The Rat Brain in Stereotaxic Coordinates*, Academic Press, San Diego (1998).
44. L. D. Lilge and B. C. Wilson, "Accuracy of interstitial measurements of absolute light fluence rate in the determination of tissue optical properties," *Proc. SPIE* **1882**, 291–304 (1993).
45. L. Wang, S. L. Jacques, and L. Zheng, "MCML—Monte Carlo modeling of light transport in multi-layered tissues," *Comput. Methods Programs Biomed.* **47**, 131–146 (1995).
46. F. A. Duck, *Physical Properties of Tissue: A Comprehensive Reference Book*, Academic Press, London (1990).
47. R. F. Tuma, G. L. Irion, U. S. Vasthare, and L. A. Heinel, "Age-related changes in regional blood flow in the rat," *Am. J. Physiol.* **249**, H485–H491 (1985).
48. K. S. Hendrich, P. M. Kochanek, J. A. Melick, J. K. Schiding, K. D. Statler, D. S. Williams, D. W. Marion, and C. Ho, "Cerebral perfusion during anesthesia with fentanyl, isoflurane, or pentobarbital in normal rats studied by arterial spin-labeled MRI," *Magn. Reson. Med.* **46**, 202–206 (2001).
49. A. Schoutens, P. Bergmann, and M. Verhas, "Bone blood flow measured by 85 Sr microspheres and bone seeker clearances in the rat," *Am. J. Physiol.* **236**, H1–H6 (1979).
50. W. C. Seyde, L. McGowan, N. Lund, B. Duling, and D. E. Longnecker, "Effects of anesthetics on regional hemodynamics in normovolemic and hemorrhaged rats," *Am. J. Physiol.* **249**, H164–H173 (1985).